Sensors & Diagnostics

PAPER

View Article Online
View Journal | View Issue

Cite this: *Sens. Diagn.*, 2024, **3**, 1476

Synthesis and characterization of La QDs: sensors for anions and H_2O_2†

Amit Sahoo and Achyuta N. Acharya *

The development of sensitive and accurate fluorescence sensors for the detection of anions and reactive oxygen species (ROS, H_2O_2) is essential as they play significant roles in biological and chemical processes. In this work, semiconductor La QDs were synthesized. The synthesized La QDs were determined to be pure with 100% La element using EDS technique. La QDs were observed in both cubic and hexagonal lattice configurations through powder XRD analysis. The morphology of the La QDs was characterized using HRTEM and FESEM data as tiny, spherical, homogenous QDs with a diameter ranging from 2 to 6 nm. The fluorescence characteristics of the synthesized La QDs were examined by studying their sensing properties that increased with an increase in anion concentration and decreased with an increase in [H_2O_2]. The variation in emission intensity at 315 nm and 440.5 nm satisfied the Stern–Volmer equation. The LOD and LOQ of H_2O_2 and anion sensing with La QDs were studied in the μM range. The Langmuir binding plots and FTIR spectra supported the concept that the surface functionalization of La QDs occurred in the presence of anions. With two band gap energies of about 3.26 eV and 4.66 eV, the synthesized La QDs are a mixture of two (binary) semiconductors.

Received 4th May 2024,
Accepted 8th July 2024

DOI: 10.1039/d4sd00142g

rsc.li/sensors

1. Introduction

Quantum dots (QDs) are highly sought owing to their size-dependent optical and electronic properties, *i.e.*, offering potential applications in nanoelectronics,[1] optoelectronics, lasers, solar cells, light-emitting diodes, and quantum computation.[2] Because of their unique optical properties and surface modification, QDs are suitable for bio-labeling and bio-imaging.[3–5] In addition, QDs have been employed in fluorescence sensing systems for a variety of analytes.[6–11] These sensors are categorized into three types: fluorescence resonance energy transfer (FRET), electron transfer, and surface-state-controlled fluorescence. The fluorescence of QDs is caused by photoinduced electron and hole recombination.[12]

Metal and semiconductor nanocrystals of size 1 to 20 nm have been synthesized using size-selective separation and solution-phase synthesis methods.[13] Singh *et al.*[14] reviewed the potentialities of bioinspired metal and metal-oxide nanoparticles in biomedical science. Body-centered cubic (BCC) structured La_2O_3 nanoparticles of size between 52 and 74 nm have been synthesized using *Moringa oleifera* leaf extract as a reducing agent *via* the photosynthesis method.[15] Lanthanum oxide nanoparticles have been synthesized from hexagonally structured lanthanum hydroxides through calcination at 600 °C for 2 h using the sonochemical method.[16] Through the sonochemical method, a new nano-sized La(III) supramolecular compound was synthesized and then calcined to 60 nm-sized lanthanum oxides at 800 °C in an ambient atmosphere.[17] La_2O_3 nanoplates and $La(OH)_3$ nanorods have been synthesized from $La(NO_3)_3{\cdot}6H_2O$ and formamide *via* facile aqueous solution synthesis at room temperature. The synthesized particles of size 14 to 18 nm have photoluminescence properties.[18] By employing atomic layer epitaxy, thin layer deposition of lanthanum oxide and stability from a β-diketonate precursor have been studied by Nieminen *et al.*[19] Glioblastoma (GBM), a deadly brain tumor with a bleak prognosis, cells may be treated with nanoparticle therapy, specifically lanthanum oxide (La_2O_3) NPs. These nanoparticles have the ability to reach the brain, dissociate, and amplify the effects of radiation therapy and chemotherapy. The cytotoxic features of NPs, which include reactive oxygen species (ROS) and apoptotic pathways, have been found to improve the therapeutic benefits of chemotherapy with temozolomide and radiation therapy.[20]

By a one-pot hydrothermal synthesis process of lanthanum oxycarbonate, hollow spheres composed of 15 nm

School of Basic Sciences & Humanities (Chemistry), Odisha University of Technology and Research, Bhubaneswar-751029, Odisha, India.
E-mail: amitsahoochemistry@gmail.com, aacharya@outr.ac.in

† Electronic supplementary information (ESI) available: Equations from E1–E4, Fig. S1–S3 and Tables from T1–T18 are submitted as ESI. See DOI: https://doi.org/10.1039/d4sd00142g

nanoparticles are fabricated using glucose, which exhibits visible luminescence.[21] On titanium, the layers of lanthanum oxycarbonate and lanthanum oxide were fabricated through electrodeposition using an organic solution. At different voltages, temperatures, and times, different-sized particle fabrication was studied.[22] Ansari *et al.* have reported the synthesis and characterization of iron lanthanum oxide nanoparticles (FeLO NPs) and their application in environmental remediation.[23] These NPs degrade industrial-grade dye up to 90%, indicating that these can be used as effective and long-lasting photocatalysts for the treatment of dye-containing waste water.[23] Hexagonal type-II $La_2O_2CO^{3+}$:Eu^{3+} nanospheres and La_2O_3:Eu^{3+} NPs were synthesized by a hydrothermal method followed by calcination at 873 K.[24] Chemo-resistive CO_2 gas sensing $La_2O_2CO_3$ nanorods of diameter 13–15 nm and length 100–150 nm were synthesized from $La(OH)_3$ nanorods by heating in a furnace at 400 °C for 2 h.[25] Nanoparticles of $La_2O_2CO_3$ of average size 35 nm, La_2O_3, and $La(OH)_3$ were prepared by a simple thermal decomposition method at 700 °C for 5 hours and were also used in photocatalytic degradation (under UV irradiation) of methyl orange dye.[26]

$LaVO_4$:Bi^{3+} was synthesized by a co-precipitation method followed by heat treatment and its luminescence properties were studied.[27] Multifunctional La-doped carbon QDs of diameter 4.3 nm were synthesized, and the quenching was also tested in the emission spectra in the presence of mercury ions.[28] Fabrication by a co-precipitation method and the photoluminescence properties of LaF_3:Eu^{3+} nanoparticles of size 12 nm were studied by Grzyb *et al.*[29] LaF_3:Ce (Ce doped LaF_3) nano powder of diameters between 40 and 15 nm and oleic acid (OA)-modified LaF_3:Ce nanoparticles of size between 5 and 10 nm were prepared through an *in situ* hydrothermal process at various concentrations of dopants.[30] Co-doped nanocrystals of LaF_3:Ce,Yb,Gd, and LaF_3:Ce have been synthesised by a chemical synthesis method, and their photoluminescence and scintillating properties have been studied by Vargas *et al.*[31] Tris(2-pyridylmethyl)amine-ligated lanthanide complexes exhibit anion-specific sensory capabilities, with the chiral ligand and lanthanide center influencing selectivity and response sensitivity.[32]

The difficulty in supramolecular anionic species recognition has become a serious problem, particularly in systems biology, catalytic processes, and analytical applications. Because anions have a lower charge-to-radius ratio and a greater propensity to establish hydrogen bonds with proton–donor liquids, developing synthetic receptors for them is difficult.[33–38] Photoinduced electron transfer (PET) sensors have been used to develop fluorescent probes that switch on for anions operating in aqueous solutions, which is a common application. These probes are developed for detecting anions and nucleotides in solutions based on PET sensors and molecular logic gates. PET anion probe development has substantially expanded the field of fluorescent probes, allowing for more accurate detection of anions and their interactions with different molecules.[39] For cellular activity and pathological states, enzymes are essential. Modern enzyme assays make use of luminous lanthanide(III) complexes, which have long luminescence lifetimes, high detection sensitivity, and line-like emission spectra for ratiometric and time-resolved studies. New strategies include polyphosphate anion luminescence signaling and anion-responsive lanthanide complexes for molecular recognition.[40] Based on dipeptides, folded-turn amido thioureas are used in a conformation switching-based fluorescence sensing technique[41–44] because of their superior ratiometric fluorescence response and increased emission of exciplex or excimer. Compounds of L-phenylalanine (L-Phe4 and L-Phe3) exhibit a stronger dual emission towards the fluoride anion.[45] Oxalate is an essential component found in plants and can harm the kidneys in the human system; it is critical for food chemistry and inductive analysis. Its high levels in the urine are a sign of pancreatic insufficiency, renal lesions, and kidney failure. The macrocyclic copper complex exhibits very selective and binding affinity ($>10^7$ M^{-1})-sensitive off–on fluorescence sensing for oxalate in water.[46] Terbium (Tb(III)) shows delayed lanthanide luminescence (luminescence of lanthanide group), with the diaryl-urea complex of Tb being significantly enhanced when dihydrogen phosphate ($H_2PO_4^-$) is recognized in an acetonitrile medium. This is due to numerous anion binding through hydrogen bonding interactions and possible metal ion coordination to Tb(III).[47]

As anions play important roles in many biological and chemical processes, the displacement approach is a strategy for building new optical anion chemosensors with high sensitivity and selectivity. Using this method, numerous good optical anion chemosensors have been developed.[48] In living systems, reactive oxygen species (ROS/RNS) play a key role. A crucial messenger in typical cell signal transduction is the stable ROS H_2O_2.[49] Imbalances in the generation of H_2O_2 result in oxidative stress and inflammation, which are associated with advanced diseases including cancer, cardiovascular problems, and Alzheimer's as well as with aging. Understanding these processes requires knowledge of how cells create and direct H_2O_2 into particular signaling pathways. Fluorescent chemosensors have been developed to monitor hydrogen peroxide, metal ions, dopamine, carbohydrates, and other physiologically relevant molecules.[48] A flexible, reusable solid-state fluoride ion sensor combines laser-patterned carbon (LP-C) and g-CNQD sensitivity, mimicking horseradish peroxidase for selective and user-friendly sensing in natural water samples.[50] Phosphate detection is crucial for biological and environmental reasons.[51] A TRF (time-resolved fluorescence)-based sensor array uses three QDs, namely, MoS_2, WS_2, and $MoSe_2$, as energy sensitizers for Tb^{3+}

$$La(NO_3)_{3(aq)} + 3NaBH_{4(aq)} \xrightarrow{0-4^{\circ}C} La_{(QDs)} + {}^{3}/_{2}\,B_2H_{6(g)} + 3NaNO_{3(aq)} + {}^{3}/_{2}\,H_{2(g)}$$

Scheme 1 Schematic of the synthesis of La QDs.

ions. CrO_4^{2-} competitively binds to Tb^{3+}, enhancing the efficiency and sensitivity in complex mixtures to phosphate detection.[52] The water-soluble cyclodextrin-modified CdSe quantum dots (β-CD-QDs) have been developed, allowing for high stability in aqueous solutions. Oxoanions such as H_2PO_4 have significant quenching effects on the fluorescence of β-CD-QDs, with Ag^+, Hg^{2+}, and Co^{2+} having significant effects.[53] CdTe QDs have been used to detect anions such as F^- in aqueous solutions for environmental monitoring, medicinal diagnostics, and *in vivo*, with high sensitivity and selectivity.[54] A CdSe–ZnS QD was surface-functionalized with 1-(2-mercapto-ethyl)-3-phenyl-thiourea and tested for selectivity towards tetrabutylammonium salts of fluoride, chloride, bromide, hydrogen sulphate, and acetate. The quench was due to an increase in the reduction potential of the receptor upon anion binding.[55]

To the best of our knowledge, no study has been reported on the one-pot synthesis of La QDs from lanthanum nitrate. In this article, we present a novel method for the simple one-pot synthesis of La QDs with high purity and yield. Lanthanum, exists at a +3 oxidation state in its nitrate salt, is reduced to 0 oxidation state and its sizes are in the range of 2–6 nm. The QDs were then characterized by XRD, XPS, HRTEM, FESEM-EDS, PCCS, and UV-visible spectroscopy (DRS). The photoluminescence properties of La QDs were studied. This study also highlights that La QDs could be considered as new optical anion chemosensors.[56] Semiconducting La QDs are used as anion chemosensors to detect anions such as F^-, Cl^-, $C_2O_4^{2-}$, CO_3^{2-}, HPO_4^{2-}, Br^-, BrO_3^-, and OH^- ions and H_2O_2 (a major ROS).

2. Experimental

2.1. Materials and methods

Lanthanum nitrate ($La(NO_3)_3{\cdot}6H_2O$, AR grade, FINAR, India) as a La(III) source and sodium borohydride ($NaBH_4$, Loba) were used as received. Millipore distilled water as a solvent (freshly prepared) for solution preparation was obtained from a Merck Millipore distillation setup.

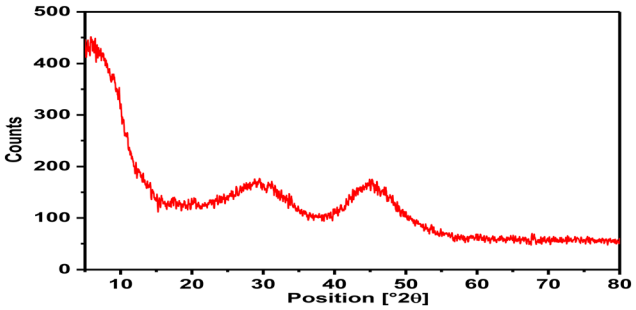

Fig. 1 XRD pattern of the synthesized La QDs.

For the X-ray diffraction (XRD) study, a Bruker D8 Advance powder XRD system was used. A JEOL FESEM (JSM-7610F) and a JEOL HRTEM (JEM-2100 Plus) were used for Field Emission Scanning Electron Microscopy (FESEM) and HRTEM studies respectively. The optical band gap energy was determined using a UV-visible spectrometer (Jasco, V-770). The PCCS study was performed using a NANOPHOX (NX0019) instrument. The luminescence studies were performed using a Jasco Make (model FP-8200) Spectrofluorometer. The surface functionalization studies were performed using a Fourier Transform Infrared (FTIR) Spectrometer (PerkinElmer, Spectrum two).

2.2. Synthesis of La QDs

First, 35 mL of 0.1 M $NaBH_4$ solution was added drop-wise into a 0.01 M lanthanum nitrate solution (~0 °C) with continuous stirring in an ice bath. The mixture was kept for 24 hours at ~10 °C (after which a grayish-white gelatinous precipitate of La QDs was formed). The gelatinous precipitate was centrifuged at 10 000 RPM for 10 minutes and dried for about 5–6 hours in an oven at 95 °C (Scheme 2).

The synthesis of La QDs from La(III) can be described by the following reaction scheme (Scheme 1):

3. Results and discussion

3.1. Characterization techniques

3.1.1. XRD study. The XRD pattern of synthesized La QDs is shown in Fig. 1. The particle size and crystalline-phase analyses of the synthesized nanoparticles were performed using a powder XRD (PXRD) instrument.[23] The unit cell

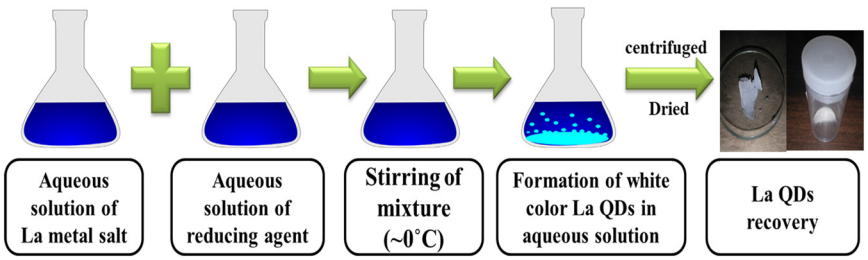

Scheme 2 Suggested steps for the synthesis of La QDs.

Table 1 XRD peak data of the synthesized La QDs

No.	2Theta [°]	FWHM [°]	*d*-Spacing [Å]	Miller indices (*h k l*) (hexagonal-La_4)	Miller indices (*h k l*) (hexagonal-La_2)	Miller indices (*h k l*) (cubic-La)	Intensity (%)	Crystalline grain size (nm)
1	29.12791	0.437333	3.06584	(0 0 4)	(— — —)	(— — —)	19.13	0.32
2	29.64268	0.068333	3.01376	(— — —)	(0 0 2)	(1 1 0)	19.29	2.09
3	31.15831	0.109333	2.87053	(1 0 2)	(1 0 1)	(— — —)	20.93	1.31
4	40.36657	0.164	2.23444	(1 0 4)	(— — —)	(— — —)	27.23	0.90
5	40.84957	0.136667	2.20913	(— — —)	(1 0 2)	(— — —)	31.66	1.08
6	42.04564	0.437333	2.14901	(— — —)	(— — —)	(2 0 0)	52.6	0.33
7	44.38562	0.068333	2.041	(0 0 6)	(— — —)	(— — —)	100	2.19

Table 2 Lattice constants of the synthesized La QDs

Crystal system	Lattice constant	Standard values (Å)	Calculated value (Å)
Hexagonal-La_4	$a = b$	3.7700	3.7602
	c	12.1590	12.2633
Hexagonal-La_2	$a = b$	3.7500	3.7483
	c	6.0700	6.0275
Cubic	$a = b = c$	4.2600	4.2621

dimensions were determined by this rapid analytical technique.

To determine the *d*-spacing (*d*) of the XRD peaks, Bragg's equation (E1) was used at λ = 0.15406 nm.[57] The *d*-spacing values of the International Centre for Diffraction Data as PDF (powder diffraction file) no.: 96-900-8526 (La_4, hexagonal), 96-900-8504 (La_2, hexagonal), and 01-089-2913 (La, cubic) were matched with the *d*-spacing values of the synthesized La QDs. The Miller indices (*h k l*) were calculated from the PDF data file.[58]

The La QDs were characterized using the PXRD data. Seven peaks between 29 and 45 (as 2θ) were taken into account for characterization. It indicates the amorphous (mixture of various crystalline states) La QDs. Seven peaks were observed, which matched well with the PDF (standard) data no.: 96-900-8526 (La_4, hexagonal), 96-900-8504 (La_2, hexagonal), and 01-089-2913 (La, cubic), and these are presented in Table 1.

From the FWHM and 2θ data of the peaks, the *d*-spacing values of each peak were calculated. The Miller indices (ESI† as E2 and E3) of the peaks were determined by matching the peak position, intensity, and *d*-spacing data of peaks with the PDF data. The crystalline grain size (ESI† as E4) of the La QDs was found to be ≈2 nm. The calculated values of the lattice constants match well with the same PDF data, and these are tabulated in Table 2.

3.1.2. XPS observation. The elemental detection and oxidation state of the elements in the synthesized La QDs were determined by the X-ray photoelectron spectroscopy (XPS) technique. The observation was made using a source analyzer at an angle of 45°. Fig. 2 shows the XPS survey spectrum of the synthesized La QDs. The XPS survey spectrum of the synthesized La QDs indicated the presence of 100% pure elementary species of lanthanum in the sample.

The high-resolution XPS spectrum of La 3d peaks is shown in Fig. 3. The dihedral peaks of La $3d_{5/2}$ and La $3d_{3/2}$ appeared in the synthesized La zero-oxidation state QDs. The La 3d peaks were observed at 836.08 eV and 852.92 eV for La $3d_{5/2}$ and $3d_{3/2}$ respectively. The satellite peaks were also observed at 839.46 eV and 856.28 eV for La $3d_{5/2}$ and La $3d_{3/2}$ respectively.[59–61]

3.1.3. HRTEM study. High-resolution transmission electron microscopy (HRTEM) (Fig. 4) was performed to examine the internal morphology of the synthesized La QDs. In this case, a 300 mesh carbon-coated copper grid (from Merck, India) was used as a reference. The HRTEM images were used to identify small spherical QDs. The average size of La QDs, as determined from the HRTEM images, is ≈2–6 nm. The Selected Area Electron Diffraction (SAED) pattern is shown in Fig. 5, which validated the high crystallinity of the La QDs. The diameter reciprocal (1/*D*), radius (*r*), *d*-spacing values and

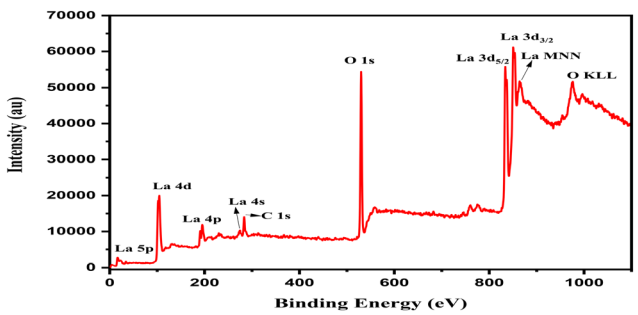

Fig. 2 XPS survey pattern of the synthesized La QDs.

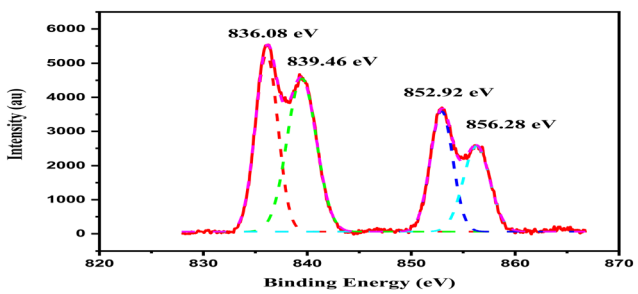

Fig. 3 La 3d high-resolution XPS pattern of the synthesized La QDs.

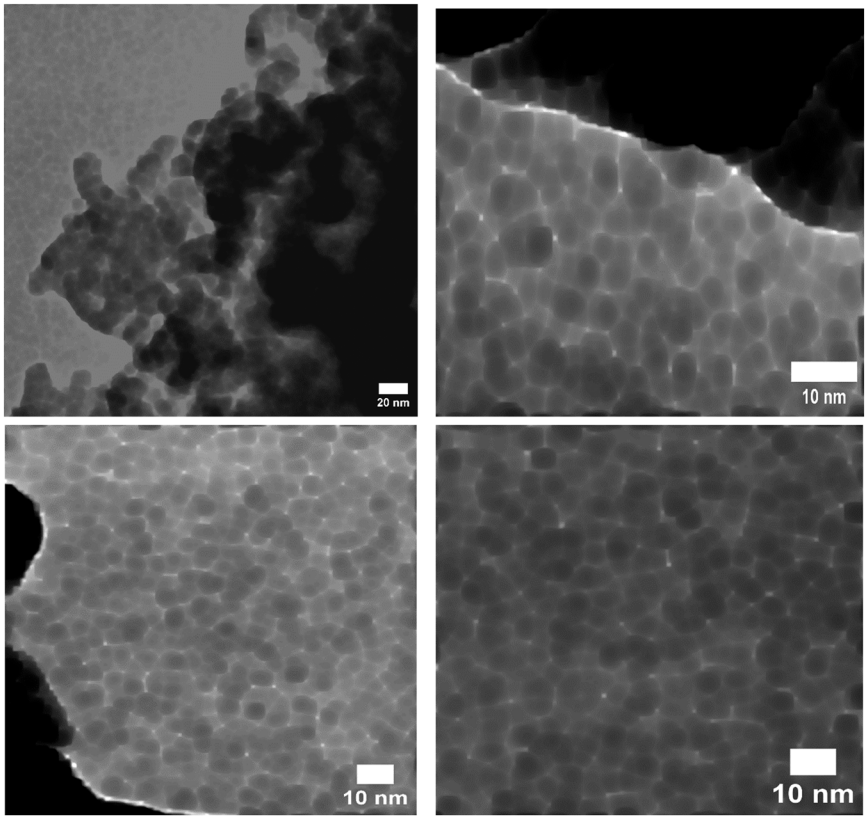

Fig. 4 HRTEM images of the La QDs.

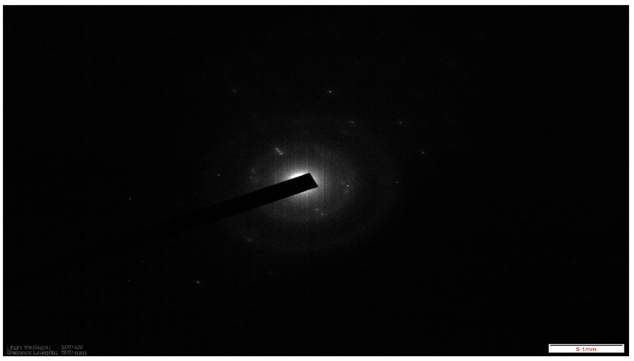

Fig. 5 SAED pattern of the La QDs.

Miller indices (h k l) matched with the d-spacing of PDF no.: 96-900-8526 (La_4, hexagonal), 96-900-8504 (La_2, hexagonal), and 01-089-2913 (La, cubic), and these are tabulated in Table 3.

3.1.4. FESEM-EDS and particle size distribution curve observation. A Field Emission Scanning Electron Microscope (FESEM) was used to characterize the surface morphology. The sample was sprayed on the surface of a carbon tape followed by gold coating for 60 s. The FESEM images of the La QDs (Fig. 6) displayed the particle sizes which are smaller, spherical, and irregular in nature. The particles are of the irregular spherical shape of average size ≈2–6 nm. The surface particle size distribution pattern is shown in Fig. 7, which shows that the particle sizes are well distributed between 1 and 10 nm range and of average size ≈2–6 nm.

The elementary nature and purity of the La QDs were determined with the help of an EDS study (Fig. 8). Between

Table 3 SAED analysis data of the synthesized La QDs

Sl no.	$1/D$ (nm^{-1})	$1/r$ (nm^{-1})	r (nm)	d-Spacing (Å)	Miller indices (h k l) (hexagonal-La_4)	Miller indices (h k l) (hexagonal-La_2)	Miller indices (h k l) (cubic-La)
1	5.693	2.8465	0.351308625	3.513086246	(— — —)	(— — —)	(— — —)
2	6.233	3.1165	0.320872774	3.208727739	(1 0 0)	(1 0 0)	(— — —)
3	6.788	3.394	0.294637596	2.946375958	(0 0 4)	(0 0 2)	(1 1 0)
4	12.307	6.1535	0.162509141	1.625091411	(2 0 0)	(2 0 0)	(2 2 0)
5	16.146	8.073	0.123869689	1.238696891	(2 1 0)	(2 1 0)	(2 2 2)
6	19.815	9.9075	0.100933636	1.009336361	(2 1 5)	(3 0 0)	(3 2 1)
7	25.076	12.538	0.079757537	0.797575371	(— — —)	(3 1 3)	(— — —)

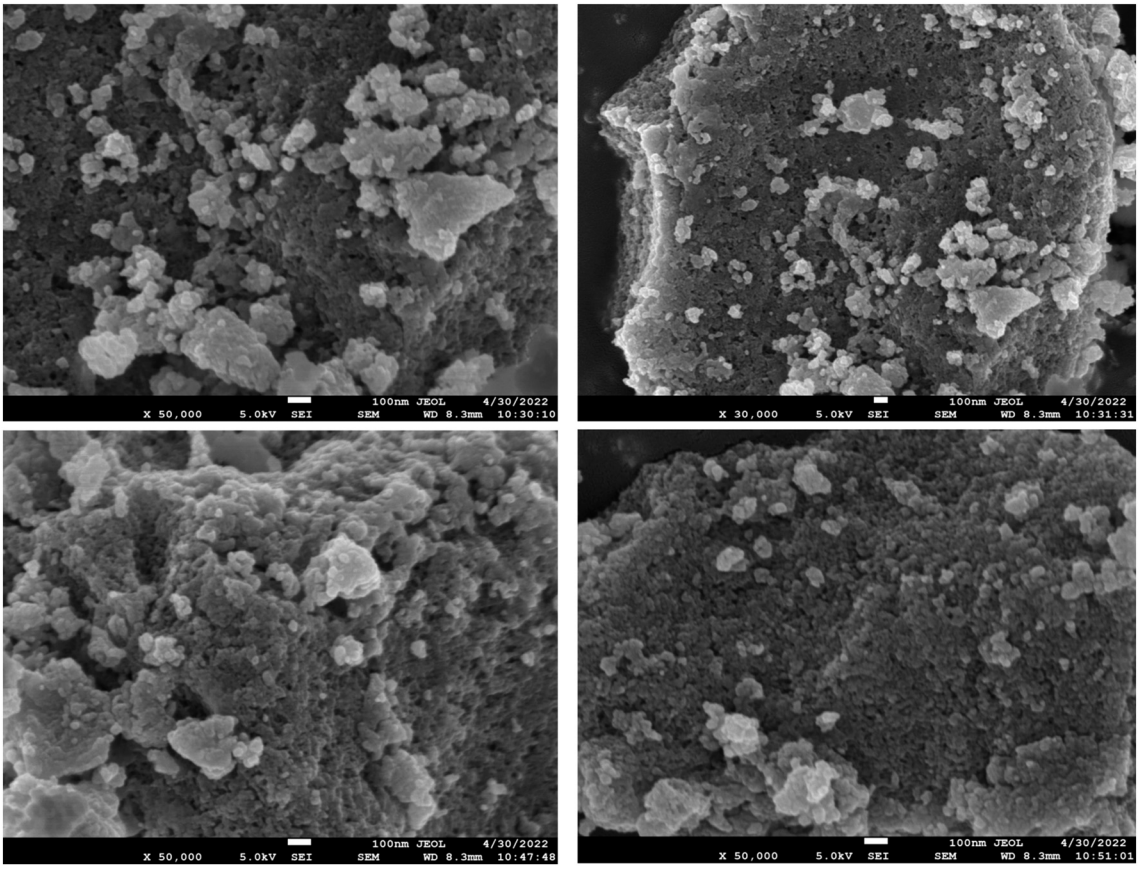

Fig. 6 FESEM images of the La QDs.

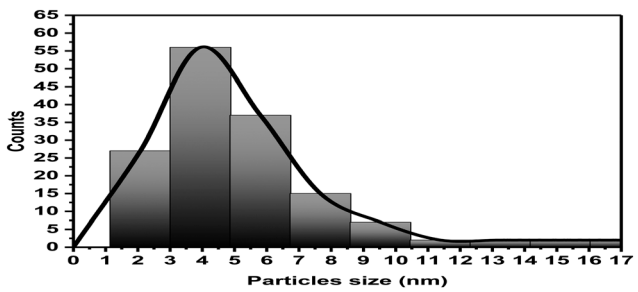

Fig. 7 Surface particle size distribution pattern of the La QDs.

the peak positions, the peaks of La QDs, in the peak position range of 0.67 to 0.99 keV, confirmed that the lanthanum is the only elementary species present in the sample with 100% purity (Table 4). The carbon peak is for the reference conductive carbon tape.

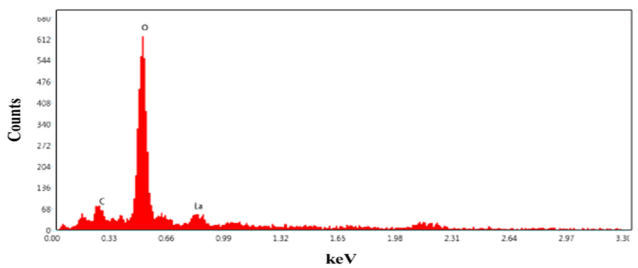

Fig. 8 EDS pattern of the La QDs.

3.1.5. PCCS observation. The particle sizes of the La QDs were analyzed by the Photon Cross-Correlation Spectroscopy (PCCS) technique, which indicates that these are non-interacting and spherical particles.[62] The density distribution of the synthesized La QDs covering the size range of 0 to 100 nm is shown in Fig. 9, and it displayed a maximum density of 1.35 q^3lg in the range of 2.4 to 5.47 nm. The size of the La QDs was determined as 2–6 nm.

3.1.6. Bandgap energy observation. The physical size of the quantum dot affects its bandgap energy.[63] The quantum confinement energy dominates the bulk semiconductor bandgap, when the dot radius decreases below the exciton Bohr radius. The direct band gap energy through the Tauc plot method (ESI† as E5) was calculated from the UV-visible (solid) spectra (Fig. 10). Two band gap energies *i.e.*, ~3.26 eV and ~4.66 eV of the La QDs, were obtained from the Tauc plot, which indicates that the La

Table 4 EDS peaks data of the synthesized La QDs

Element	Weight%	Atomic%	Net int.
C K	7.39	17.04	17.70
O K	42.08	72.87	128.83
La M	50.54	10.08	9.50

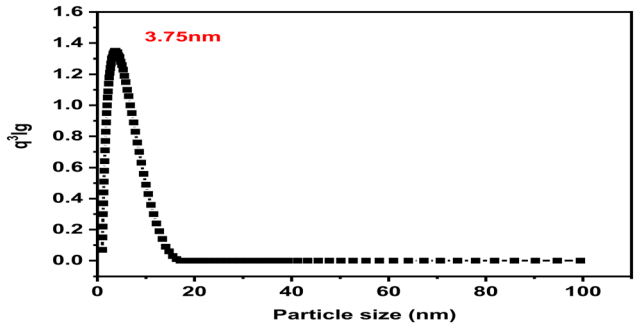

Fig. 9 Density distribution spectra of La QDs.

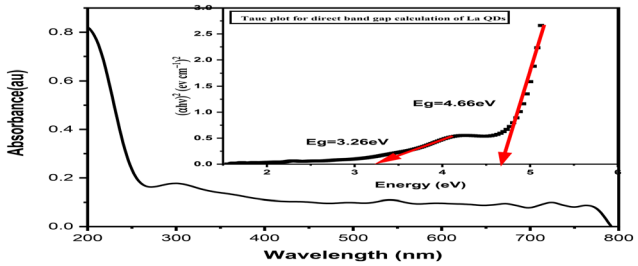

Fig. 10 UV-visible spectra with the Tauc plot of La QDs.

QDs are a mixture of two semiconductor QDs. The conversion of band gap energies (eV) to wavelengths (nm) is given in Table 5.

3.1.7. Spectrofluorometric observation. The luminescence properties based on the specific emission and excitation wavelengths of the La QDs were studied, where 10 ppm dispersed La QDs in ethanol was used. Upon excitation at 265 nm wavelength, the La QDs exhibit two emission peaks at 315 nm and 440.5 nm (Fig. 11b), which have an absolute quantum yield of ~71%.[64] The La QDs with a maximum intensity emission peak at 315 nm wavelength gives an excitation peak at 265 nm (Fig. 11a). The La QDs give one emission peak at 438.5 nm wavelength (Fig. 12b), one excitation peak at 382.5 nm wavelength and also two excitation peaks at 265 nm and 382.5 nm wavelengths (Fig. 12a), one emission peak at 438.5 nm wavelength. The analysis of band gap energies indicated (Table 5) two excitation wavelengths at 265 nm and 382.5 nm for the semiconductor La QDs. Upon excitation at 265 nm (bearing high energy (eV)), it gives two emission peaks (Fig. 11b). The naked-eye visual of the La QDs in ethanol under UV irradiation is provided in the S1 ESI.† Wu *et al.*[65] reported that when the dispersion was excited at various wavelengths from 240 to 500 nm, the PL spectra

Table 5 Data on the conversion of band gap energies (eV) to wavelengths (nm) of the synthesized La QDs

No.	Band gap energy (eV)	Wavelength (nm)
1	3.26	380.32
2	4.66	266.06

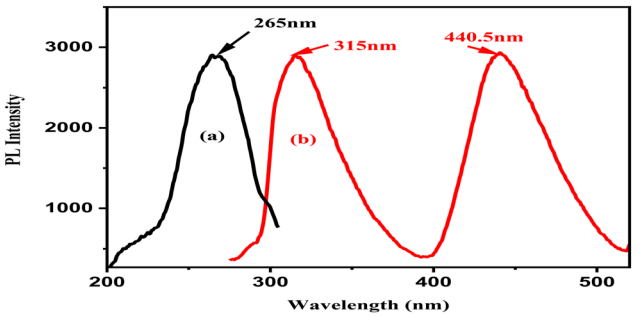

Fig. 11 (a) Excitation spectra of the La QDs in ethanol with a maximum emission at 315 nm wavelength. (b) Emission spectra of the La QDs in ethanol with an excitation at 265 nm wavelength.

exhibited a red-shift for β-SiC nanocrystallites with diameters in the range of 1–6 nm in an aqueous medium, which is due to the quantum confinement effect, *i.e.*, the PL peak positions display red-shift as the excitation wavelength increases.[65–68] Similarly, the PL spectra of La QDs also exhibited the red-shift when excited at various wavelengths between 250 and 470 nm (Fig. 13(a) and (b)). These findings are illustrated more clearly in Fig. 13(c), where the PL peak positions are plotted against the excitation wavelength. These results support the quantum confinement effect of the La QDs. Based on this, the La QDs are used as sensors for H_2O_2 and various anions, *i.e.*, F^-, Cl^-, $C_2O_4^{2-}$, CO_3^{2-}, HPO_4^{2-}, Br^-, BrO_3^-, and OH^- ions.

3.1.8. Calibration curves of various anions: (i) F^-, Cl^-, $C_2O_4^{2-}$, CO_3^{2-}, HPO_4^{2-}, Br^-, BrO_3^-, and OH^- ions and (ii) H_2O_2 sensor. The La QDs are used as sensors for various anions, *i.e.*, F^-, Cl^-, $C_2O_4^{2-}$, CO_3^{2-}, HPO_4^{2-}, Br^-, BrO_3^-, and OH^- ions using four equations and they are (i) the Stern–Volmer equation (eqn (1)), (ii) linear fit equation (eqn (2)), (iii) exponential (asymptotic) curve fit equation (eqn (3)), and (iv) Langmuir equation of binding (eqn (4)):

$$I_0/I = 1 \pm K_{sv}[Q] \quad (1)$$

$$y = A + Bx \quad (2)$$

$$Y = A - BC^X \quad (3)$$

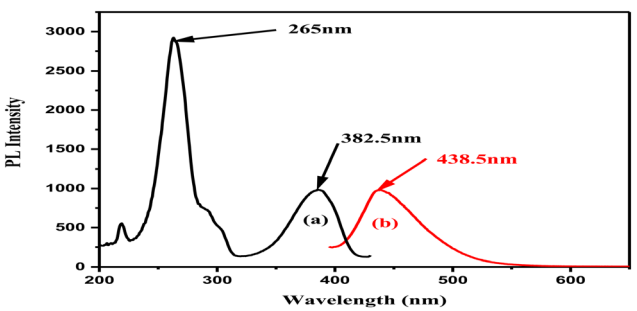

Fig. 12 (a) Excitation spectra of the La QDs in ethanol with a maximum emission at 438.5 nm wavelength. (b) Emission spectra of the La QDs in ethanol with an excitation at 382.5 nm wavelength.

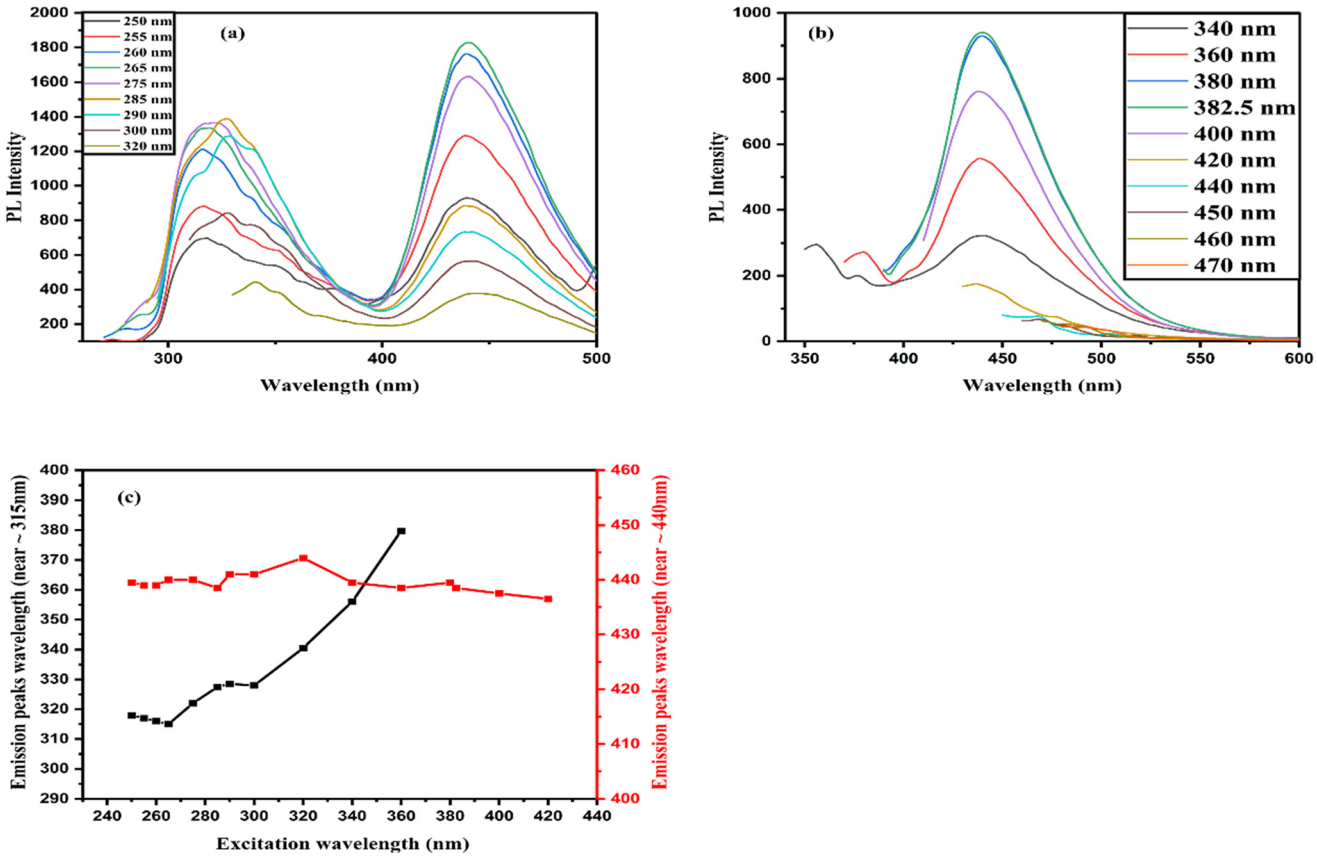

Fig. 13 PL spectra of La QDs obtained (a) at nine distinct excitation wavelengths between 250 and 320 nm and (b) at ten distinct excitation wavelengths between 340 and 470 nm. (c) PL peak position of La QDs concerning the excitation wavelength.

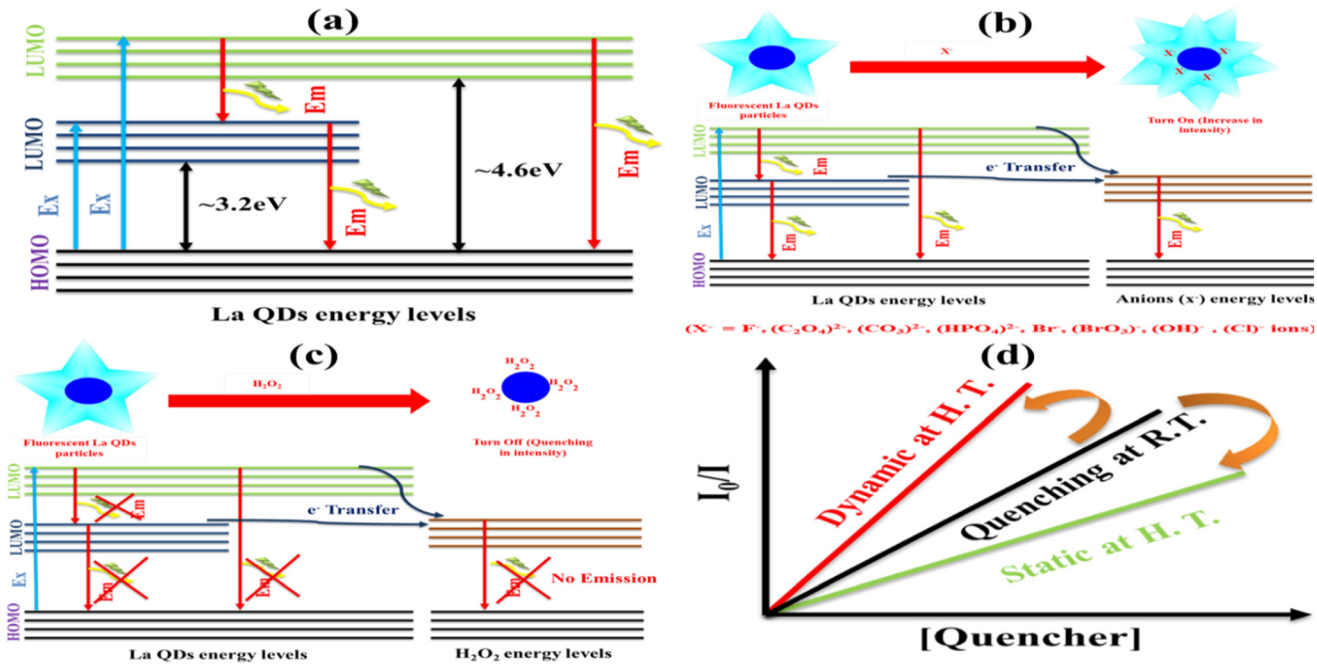

Fig. 14 Schematic of the fluorescence mechanism of (a) La QDs in sensing (b) anions and (c) H_2O_2. (d) Comparison between static and dynamic quenching.

Table 6 Comparative study of the sensing of anions and H_2O_2 with QDs

Sl. no.	Materials (QDs)	Anions/H_2O_2	Sensing capacity data and fluorescence turn on/off	Ref.
1	Carbon quantum dots (CQDs)	H_2O_2	0–88 mM at 604 nm emission (Em) peak 0–66 mM at 570 nm emission (Em) peak Fluorescence turn off	71
2	Zr QDs	H_2O_2	0–2.5 M at 406 and 430 nm Em peaks 0–0.15 M at 413 nm Em peak Fluorescence turn off	64
3	CQDs@gum Arabic-silver nanoparticles	H_2O_2	0–2.2 mM at 520 nm Em peak Fluorescence turn on	72
4	Chicken cartilage carbon dots	H_2O_2	2–3000 μM at 435 nm Em peak Fluorescence turn off 0.47 μM LOD	73
5	CdTe QDs-Ca^{2+}	F^-	0–12 mM at 600 nm Em peak Fluorescence turn on	74
6	Thioglycolic acid capped CdTe QDs	H_2O_2	0–200 μM [H_2O_2] at 550 nm Em peak Fluorescence turn off	74
		SO_3^{2-}	0–7.6 mM [SO_3^{2-}] at 550 nm Em peak Fluorescence turn on	
		PO_4^{3-}	0–1.6 mM [PO_4^{3-}] at 550 nm Em peak Fluorescence turn on	
7	β-CD-QDs	$H_2PO_4^-$, OH^-, HPO_4^{2-}, PO_4^{3-}	0–0.001 mol L^{-1} [anions] at 410 nm Em peak Fluorescence turn off	39
8	Thioglycolic acid-capped CdTe QDs	F^-, $C_2O_4^{2-}$, CO_3^{2-} H_2O_2	Fluorescence turn on Fluorescence turn off	3
9	CdTe QDs	CO_3^{2-}	0–123.5 μM at 560 nm Em peak Fluorescence turn on	75
10	CdSe-ZnS QD	AcO^-, F^-, Cl^-, Br^-, HSO_4^-	Fluorescence turn off	41

$$[C]/I = (1/I_0)[C] + (1/BI_0) \quad (4)$$

where 'x' denotes the concentration of anions (F^-/Cl^-/$C_2O_4^{2-}$/CO_3^{2-}/HPO_4^{2-}/Br^-/BrO_3^-/OH^- or H_2O_2) and 'y' represents the intensity (eqn (2) and (3)). In eqn (1), I_0 is the PL intensity of QDs at zero concentration of H_2O_2 and anions, I is the PL intensity at [Q] of F^-/Cl^-/$C_2O_4^{2-}$/CO_3^{2-}/HPO_4^{2-}/Br^-/BrO_3^-/OH^-/H_2O_2, and K_{sv} and $-K_{sv}$ are the Stern–Volmer quenching constant and Stern–Volmer enhancement constant respectively. In eqn (4), [C] denotes the concentration of F^-/Cl^-/$C_2O_4^{2-}$/CO_3^{2-}/HPO_4^{2-}/Br^-/BrO_3^-/OH^-/H_2O_2, I_0 is the PL intensity of QDs at zero concentration of anions, I is the PL intensity of QDs at a concentration of anions denoted as [C], and B denotes the Langmuir binding constant.

The limit of detection (LOD) and limit of quantification (LOQ)[69] of the anions and H_2O_2 sensors were calculated using eqn (5) and (6) respectively as follows:

$$LOD = 3.3 \times (\sigma/s) \quad (5)$$

$$LOQ = 10 \times (\sigma/s) \quad (6)$$

where σ is the standard deviation and s is the slope.

In Fig. 14(a–c), the fluorescence mechanism, used for La QDs in the sensing of anions and H_2O_2, emphasizes electronic transitions and the relationship between emission peaks and band gap energies. The quenching of La QD fluorescence occurs in the presence of H_2O_2. At room temperature (R.T.), the quenching behavior, *i.e.*, the decrease in PL intensity of La QDs with the increase in the concentration of H_2O_2, satisfies the linearity of the Stern–Volmer equation. With the increase in temperature (at high temperature, H.T.), molecules move more quickly and diffuse, which leads to huge collisional events that are best represented by dynamic quenching. In contrast, in the case of static quenching, the complex dissociates (losing its bonds) with the increase in temperature (Fig. 14(d)).[70]

3.1.9. Sensing properties

3.1.9.1. Anion sensing properties (F^-, Cl^-, $C_2O_4^{2-}$, CO_3^{2-}, HPO_4^{2-}, Br^-, BrO_3^-, and OH^-). The fluorescence studies for sensing anions were conducted at room temperature upon excitation at 265 nm with different micromolar concentrations of the anions, *i.e.*, $0 \le [F^-]$, μM ≤ 228.57; $0 \le [Cl^-]$, μM ≤ 171.42; $0 \le [C_2O_4^{2-}]$, μM ≤ 142.85; $0 \le [CO_3^{2-}]$, μM ≤ 228.57; $0 \le [HPO_4^{2-}]$, μM ≤ 85.71; $0 \le [Br^-]$, μM ≤ 171.42; $0 \le [BrO_3^-]$, μM ≤ 200; and $0 \le [OH^-]$, μM ≤ 200. In all the cases, the fluorescence intensity of the anion sensors increases significantly (Table 6) with the increase in [anions].[2,32,33] The FL intensity spectra of F^-, CO_3^{2-}, HPO_4^{2-}, and OH^- sensors are presented in Fig. 15. The FL intensity spectra for other anions are included in the ESI† as S2. Similarly, the calibration curves of the F^-, CO_3^{2-}, HPO_4^{2-}, and OH^- sensors are shown in Fig. 16, and the calibration of the rest of the anions is included in the ESI† as S3.

The intensity of emission increases linearly (eqn (2)) with the increase in [F^-] for both peaks at 315 nm and

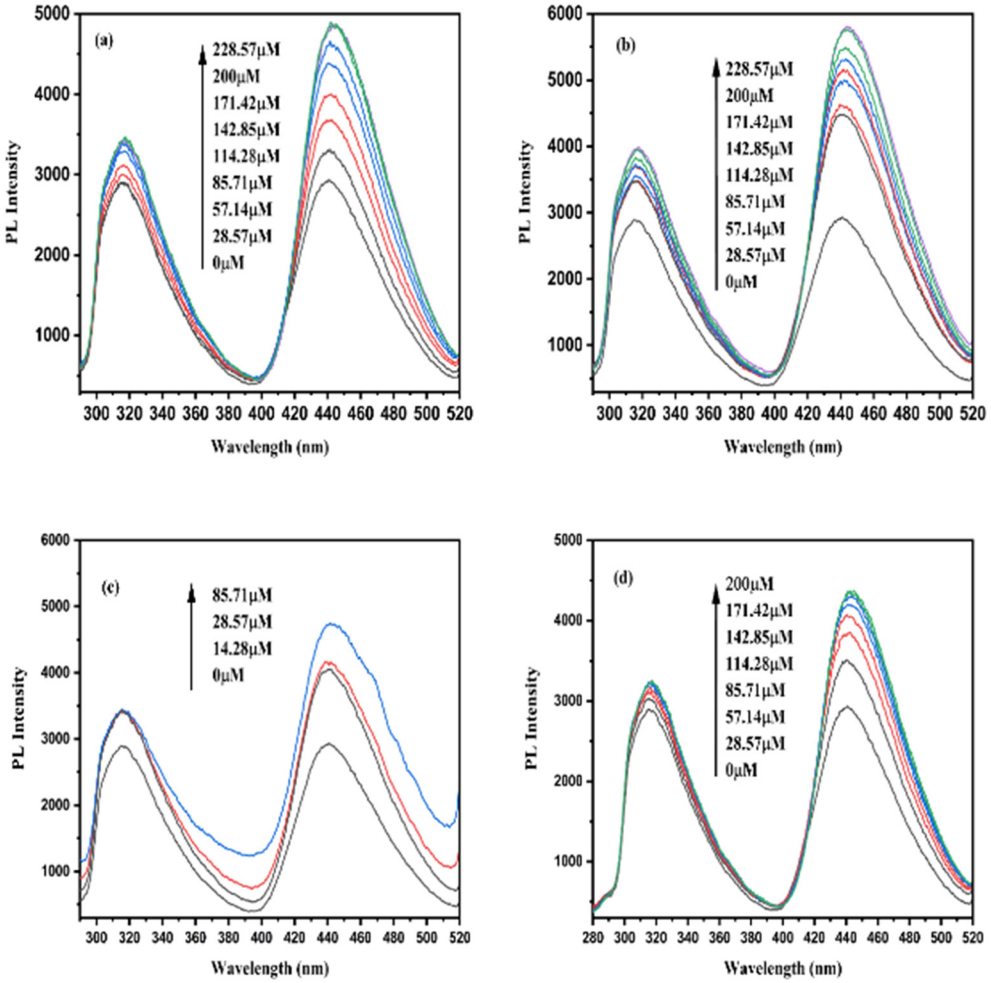

Fig. 15 Emission spectra of the optical La QD sensor at 315 and 440.5 nm wavelength upon excitation at 265 nm with different (a) [F^-], (b) [CO_3^{2-}], (c) [HPO_4^{2-}], and (d) [OH^-].

440.5 nm (Fig. 16) (ESI† in T1). The intensity of emission increases exponentially (eqn (3)) concerning the concentration increase of Cl^-, $C_2O_4^{2-}$, CO_3^{2-}, HPO_4^{2-}, Br^-, BrO_3^-, and OH^- ions, which is presented in Fig. 17 and ESI† (S3 and T2–T8).

The enhancement in the intensities of the emission spectra concerning the concentration increase of F^-, Cl^-, $C_2O_4^{2-}$, CO_3^{2-}, HPO_4^{2-}, Br^-, BrO_3^-, and OH^- ions satisfied the Stern–Volmer equation (eqn (1)), which is shown in Fig. 17 (ESI† in T9–T16). The Langmuir binding plots (eqn (4)) of the F^-, Cl^-, $C_2O_4^{2-}$, CO_3^{2-}, HPO_4^{2-}, Br^-, BrO_3^-, and OH^- ions for the surface functionalization of the La QDs are depicted in Fig. 18.

3.1.9.2. H_2O_2 sensing properties. At room temperature and 40 °C, the fluorescence studies for sensing H_2O_2 (due to quenching) were conducted ($0 \leq [H_2O_2]$, mM ≤ 25.2) upon excitation at 265 nm (Fig. 19) wavelength. The fluorescence intensity of the H_2O_2 sensors decreases significantly (Table 6) with the increase in $[H_2O_2]$. The calibration curves of the H_2O_2 sensors at both room temperature and 40 °C are shown in Fig. 20(a) and (b) respectively.

At the 315 nm and 440.5 nm peaks, the intensity of emission decreases exponentially (eqn (3)) concerning the increase in $[H_2O_2]$, which is shown in Fig. 20(a) and (b) (ESI† in T17). At the 315 nm and 440.5 nm wavelengths, the quenching in the intensities of the emission spectra concerning the $[H_2O_2]$ satisfied the Stern–Volmer equation (eqn (1)), which is shown in Fig. 20(c) and (d) (ESI† in T18). The Stern–Volmer plot of the H_2O_2 sensor shows a downward shift at high temperatures with respect to the room-temperature fit plot of the same at both emission peaks. Hence, the H_2O_2 sensors of La QDs support the static quenching (Fig. 14(d)) mechanism.

3.1.9.3. Selectivity of La QD sensors for anions. The fluorescence intensity of La QDs was studied in the presence of F^-, $C_2O_4^{2-}$, CO_3^{2-}, HPO_4^{2-}, Br^-, BrO_3^-, OH^- and Cl^- anions. The I_0/I values at 315 nm (Fig. 21(a)) and 440.5 nm (Fig. 21(b)) emission peaks for each anion are presented in the form of a bar graph at fixed concentrations of all the anions at 28.57 μM. The minimum I_0/I value is found in the case of CO_3^{2-} ions,

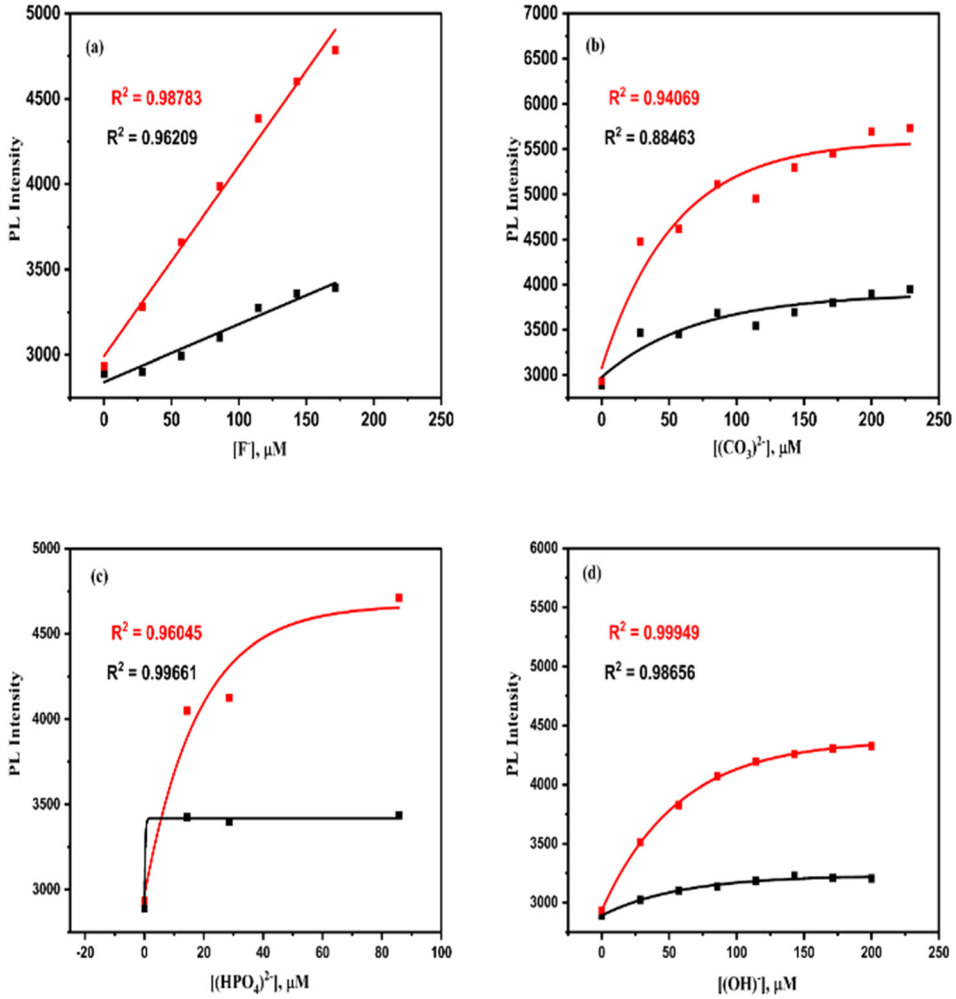

Fig. 16 Calibration curves for various sensors at 315 and 440.5 nm wavelengths: (a) F^-, (b) CO_3^{2-}, (c) HPO_4^{2-}, and (d) OH^-.

i.e., the enhancement of the fluorescence intensities is maximum in the presence of CO_3^{2-} ions. This indicates that the synthesized La QDs can be used as better selective sensors for CO_3^{2-} ions. Similarly, the maximum I_0/I values at 315 nm (Fig. 21(a)) and 440.5 nm (Fig. 21(b)) emission peaks in the presence of H_2O_2 are observed at a concentration of 2.8 mM. The quenching of the fluorescence intensities is maximum in the case of H_2O_2. A bar graph representing the I_0/I value for CO_3^{2-} ion emission peaks at a fixed concentration of 28.57 μM is presented at temperatures of −10 °C, ~25 °C (room temperature), and 40 °C (Fig. 21d). The I_0/I value is found to be lowest at room temperature, indicating that the synthesized La QDs can be employed as more selective CO_3^{2-} ion sensors at this temperature. Similar temperature variation studies were also conducted for H_2O_2 (2.8 mM) quenching and the I_0/I values were found to be maximum at both −10 °C and at room temperature (Fig. 21c). This indicates that H_2O_2 quenching is effective at both room temperature and lower temperatures of −10 °C.

Langmuir binding constants for anions for the surface functionalization of the La QDs are given in Table 9. The increasing order of Langmuir binding constants (B) (Table 8, ESI† in T19) of anions with La QDs at 315 nm excitation wavelength is $CO_3^{2-} < F^- \approx Cl^- < BrO_3^- < OH^- < C_2O_4^{2-} < Br^- < HPO_4^{2-}$. The increasing order of Langmuir binding constants (B) (Table 9) of anions with La QDs at 440.5 nm excitation wavelength is $F^- \approx Cl^- < CO_3^{2-} < OH^- < BrO_3^- < Br^- < C_2O_4^{2-} < HPO_4^{2-}$. Langmuir binding plot is not fitted for the H_2O_2 sensing, which supports the agglomeration (no surface functionalization or, no binding) of La QDs in the presence of H_2O_2.[76,77] The surface functionalization of La QDs in the presence of anions in an ethanol medium was examined by employing the FTIR spectra (Fig. 22). The two peaks appeared at ~1049.29 cm^{-1} and ~1087.87 cm^{-1}, which may be for the interaction of La QDs with ethanol.[78,79] Due to the surface functionalization of La QDs in the presence of anions, the peak at ~1049.29 cm^{-1} is shifted to ~1046.4 cm^{-1} for CO_3^{2-}, HPO_4^{2-}, and BrO_3^- anions; ~1048.32 cm^{-1}

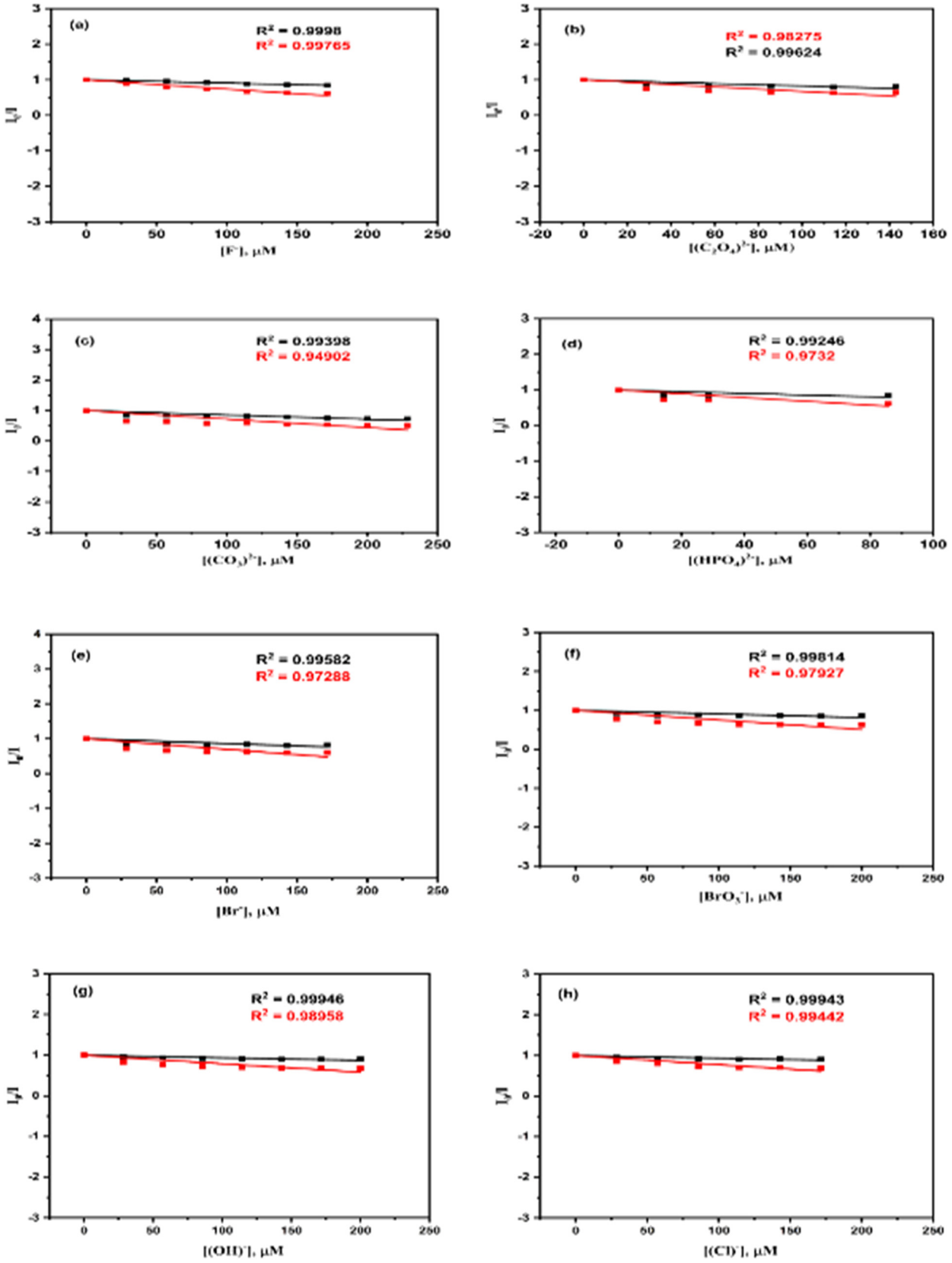

Fig. 17 Stern–Volmer plots for various sensors at 315 and 440.5 nm wavelengths: (a) F^-, (b) $C_2O_4^{2-}$, (c) CO_3^{2-}, (d) HPO_4^{2-}, (e) Br^-, (f) BrO_3^-, (g) OH^-, and (h) Cl^-.

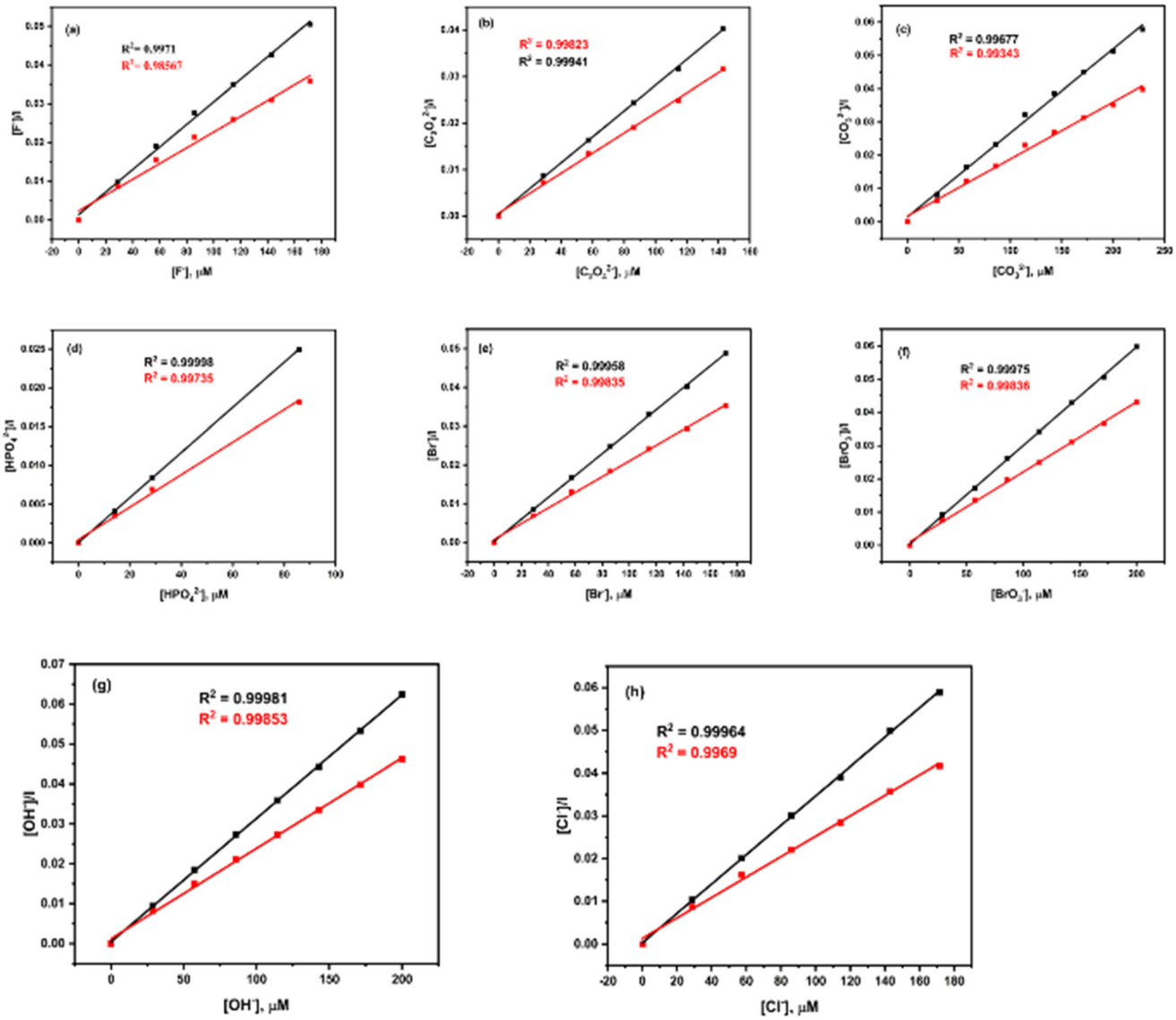

Fig. 18 Langmuir binding plots for various sensors at 315 and 440.5 nm wavelengths: (a) F^-, (b) $C_2O_4^{2-}$, (c) CO_3^{2-}, (d) HPO_4^{2-}, (e) Br^-, (f) BrO_3^-, (g) OH^-, and (h) Cl^-.

and ~1050.25 cm^{-1} for Br^- and Cl^- ions respectively. Similarly the peak at ~1087.87 cm^{-1} is also shifted to ~1086.90 cm^{-1} (CO_3^{2-}), ~1090.76 cm^{-1} (HPO_4^{2-}), ~1089.79 cm^{-1} (Br^-) and ~1088.83 cm^{-1} (BrO_3^-) in the presence of anions. The peak at ~1087.87 cm^{-1} of La QDs is not shifted and one new broad peak appeared at ~1021.32 cm^{-1} in the presence of Cl^- anions.

The K_{sv} values were determined, and are presented in Table 7. The LOD (eqn (5)) and LOQ (eqn (6)) values of sensing were calculated,[69] and are also presented in Table 7. The stability constants of anions with La(III) ions were obtained from the literature and are presented in Table 8, and it is highest for CO_3^{2-} anions. The I_0/I value was found to be minimum at both the wavelengths (315 and 440.5 nm), indicating that La QDs were found to be better anion sensors for CO_3^{2-} anions. The increasing order of Stern–Volmer constants (K_{sv}) (Table 7) of anions with La QDs at 315 nm excitation wavelength is $OH^- < Cl^- < F^- < BrO_3^- < Br^- < CO_3^{2-} < C_2O_4^{2-} < HPO_4^{2-}$, and the same at 440.5 nm excitation wavelength is $OH^- < Cl^- < BrO_3^- < F^- < CO_3^{2-} < Br^- < C_2O_4^{2-} < HPO_4^{2-}$.

4. Conclusion

In summary, a one-pot chemical reduction method has been adopted to synthesize semiconductor La QDs utilizing sodium borohydride as a reducing agent at ~0 °C. La QDs are a mixture of cubic (La), hexagonal (La_4), and hexagonal (La_2) crystalline forms, according to the XRD pattern analysis. The small, spherical, homogeneous La QDs are said to have a specific shape with the QDs

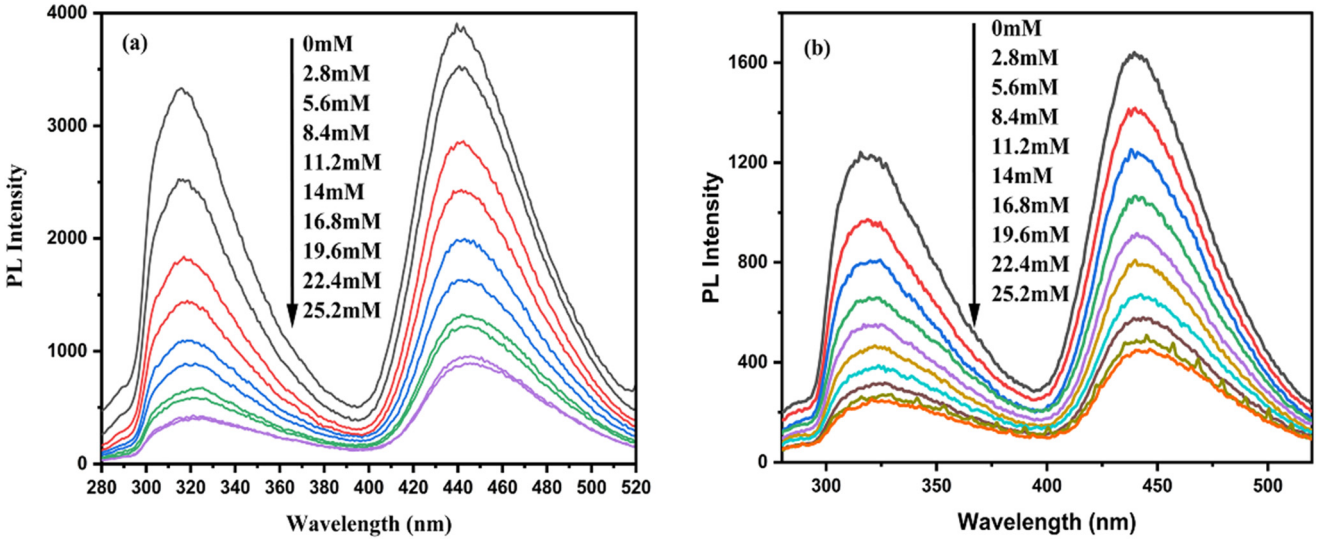

Fig. 19 Emission spectra of the optical La QD sensor under different [H_2O_2] at 315 nm and 440.5 nm wavelengths: (a) at room temperature, and (b) at 40 °C.

2–6 nm in size. The FESEM and HRTEM data indicated that the surface QD size is also 2–6 nm. The EDS data indicated ~100% purity of the synthesized La QDs. La QDs have two band gap energies of ~3.26 eV and

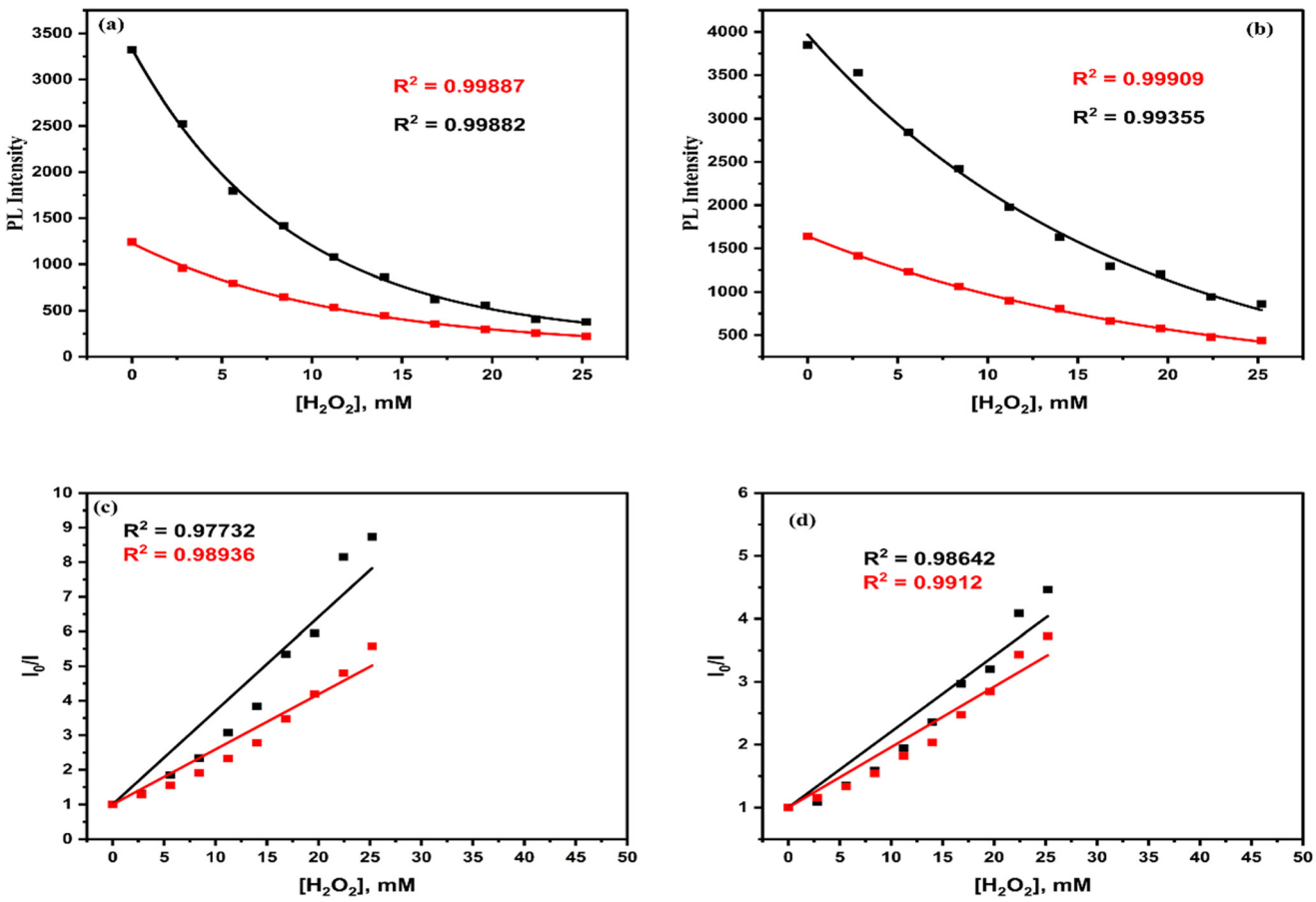

Fig. 20 Calibration curves of H_2O_2 sensor peaks at: (a) 315 nm, and (b) 440.5 nm wavelengths. Stern–Volmer plots of H_2O_2 sensor peaks at: (c) 315 nm, and (d) 440.5 nm wavelengths.

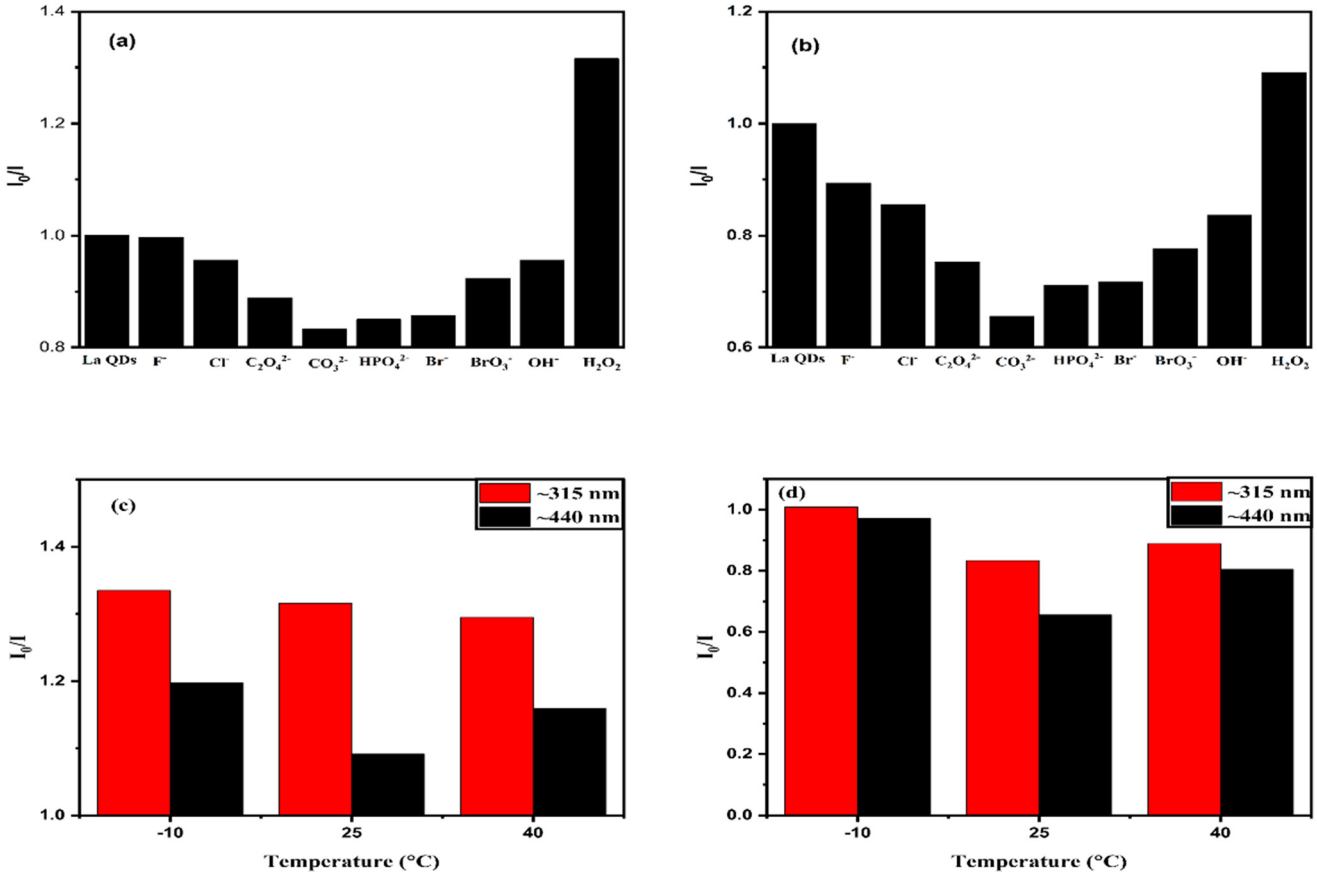

Fig. 21 (a) Selectivity of the La QD sensors for F^-, $C_2O_4^{2-}$, CO_3^{2-}, HPO_4^{2-}, Br^-, BrO_3^-, OH^-, Cl^- and H_2O_2 at 315 nm wavelength at room temperature. (b) Selectivity of the La QD sensors for F^-, $C_2O_4^{2-}$, CO_3^{2-}, HPO_4^{2-}, Br^-, BrO_3^-, OH^-, Cl^- and H_2O_2 at 440.5 nm wavelength at room temperature. (c) Selectivity of the La QD sensors for H_2O_2 at 315 nm and 440.5 nm wavelengths at different temperatures. (d) Selectivity of the La QD sensors for CO_3^{2-} at 315 nm and 440.5 nm wavelengths at different temperatures.

~4.66 eV, which qualifies them as a mixture of semiconductors. The La QDs are anion sensors for the anions F^-, Cl^-, $C_2O_4^{2-}$, CO_3^{2-}, HPO_4^{2-}, Br^-, BrO_3^-, and OH^- and relatively better sensors for CO_3^{2-}. Due to the static quenching of La QDs in the presence of H_2O_2, it could act as a H_2O_2 sensor. It may be used for sensing one of the ROS in the biological system.

The sensing properties of La QDs in biological science may be applied due to its high selectivity for carbonate anion and H_2O_2. Initial studies on La QDs showed its ability to sense carbohydrates and bioconjugate DNA/RNA characteristics. These investigations are ongoing, and the findings will be published at a later date.

Table 7 Stern–Volmer constant values with LOD and LOQ values for sensing F^-, $C_2O_4^{2-}$, CO_3^{2-}, HPO_4^{2-}, Br^-, BrO_3^-, OH^-, and Cl^- ions and H_2O_2 at 315 nm and 440.5 nm wavelengths

Anions	10^3K_{sv}, μM^{-1} (λ = 315 nm)	10^3K_{sv}, μM^{-1} (λ = 440.5 nm)	λ = 315 nm (in μM)		λ = 440.5 nm (in μM)	
			LOD	LOQ	LOD	LOQ
F^-	0.89 (±0.05)	2.6 (±0.1)	29.6	89.8	34.7	105
$C_2O_4^{2-}$	1.72 (±0.24)	3.26 (±0.5)	89.9	272	97.9	297
CO_3^{2-}	1.43 (±0.1)	2.79 (±0.3)	105	317	135	410
HPO_4^{2-}	2.41 (±0.9)	5.32 (±1)	146	441	87.1	264
Br^-	1.38 (±0.22)	3.06 (±0.4)	128	388	116	351
BrO_3^-	0.92 (±0.1)	2.47 (±0.3)	115	347	115	348
OH^-	0.64 (±0.06)	2.1 (±0.24)	83.5	253	96.1	291
Cl^-	0.67 (±0.08)	2.24 (±0.2)	103.4	313	69.7	211
H_2O_2	270 (±16) × 10^{-3}	120 (±6) × 10^{-3}	3906	11 836	3496	10 593

Table 8 Stability constant of anions with the La(III) ion with the I_0/I values of La QDs in the presence of anions at a concentration of 28.57 μM at 315 nm and 440.5 nm wavelengths

Anions	Stability constants ($\log_{10}$)	Ref.	I_0/I (315 nm)	I_0/I (440.5 nm)
F^-	3.12	80	0.99623	0.89364
$C_2O_4^{2-}$	6	81	0.8883	0.7527
CO_3^{2-}	6.82	80	0.8336	0.65533
HPO_4^{2-}	4.87	80	0.85013	0.7112
Br^-	0.42	82	0.85654	0.71718
BrO_3^-	—	—	0.9235	0.77634
OH^-	5.1	80	0.9561	0.83539
Cl^-	0.29	80	0.95563	0.85511

Table 9 Langmuir binding constants of La QDs for F^-, $C_2O_4^{2-}$, CO_3^{2-}, HPO_4^{2-}, Br^-, BrO_3^-, OH^-, and Cl^- ions at 315 nm and 440.5 nm wavelengths

Anions	Binding constant (B) (315 nm wavelength)	Binding constant (B) (440.5 nm wavelength)
F^-	0.20337 ($\pm0.97 \times 10^{-2}$)	0.08468 ($\pm0.96 \times 10^{-2}$)
$C_2O_4^{2-}$	0.7226 ($\pm1.15 \times 10^{-2}$)	0.35475 ($\pm1.15 \times 10^{-2}$)
CO_3^{2-}	0.17071 ($\pm0.73 \times 10^{-2}$)	0.09915 ($\pm0.73 \times 10^{-2}$)
HPO_4^{2-}	9.88063 ($\pm2.18 \times 10^{-2}$)	0.48755 ($\pm2.18 \times 10^{-2}$)
Br^-	0.7709 ($\pm0.97 \times 10^{-2}$)	0.23985 ($\pm0.97 \times 10^{-2}$)
BrO_3^-	0.68201 ($\pm0.83 \times 10^{-2}$)	0.20024 ($\pm0.83 \times 10^{-2}$)
OH^-	0.68986 ($\pm0.83 \times 10^{-2}$)	0.18893 ($\pm0.83 \times 10^{-2}$)
Cl^-	0.20337 ($\pm0.97 \times 10^{-2}$)	0.08468 ($\pm0.97 \times 10^{-2}$)

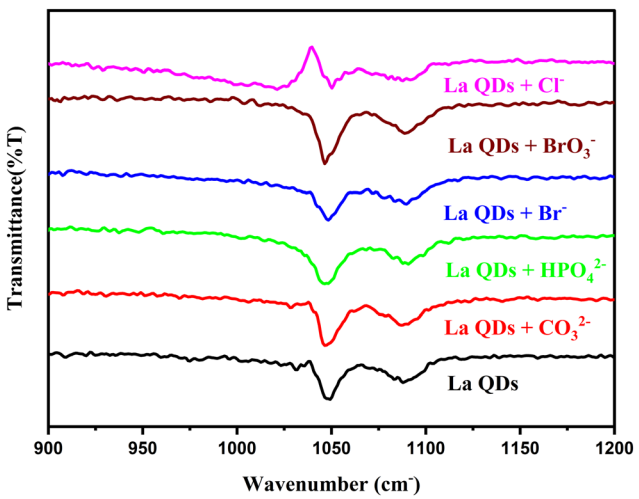

Fig. 22 Stack FTIR spectra of the La QD sensor in the presence of different anions.

Data availability

As per the norms of the journal, the data will be provided on request.

Author contributions

The study's conception and design were aided by A. N. A. and A. S. Data interpretation had been conducted by A. N. A. The manuscript was drafted by A. N. A. and A. S.

Conflicts of interest

The authors declare no conflicts of interest and claim their work is original, unpublished, and not under consideration for publication elsewhere.

Acknowledgements

With assistance from the Department of Chemistry, ICT-IOC, Bhubaneswar, India, the XRD, FESEM, EDS and HRTEM characterizations were completed. With the aid of the Institute Instrumentation Centre (IIC), IITR, Roorkee, India, the XPS characterization is completed. Regarding their assistance in characterizing La QDs, the authors expressed their gratitude.

References

1 H. I. Alrayzan, S. A. Ansari and N. Parveen, *J. Nanoelectron. Optoelectron.*, 2022, **17**, 536–543.
2 M. Bottrill and M. Green, *Chem. Commun.*, 2011, **47**, 7039–7050.
3 S. Ye, F. Su, J. Li, B. Yu, L. Xu, T. Xiong, K. Shao and X. Yuan, *J. Mater. Chem. B*, 2024, **12**, 122–130.
4 X. Cai, B. Wang, L. Nian, S. Zhao and J. Xiao, *J. Mater. Chem. B*, 2023, **12**, 1031–1042.
5 A. Tiwari, S. Walia, S. Sharma, S. Chauhan, M. Kumar, T. Gadly and J. K. Randhawa, *J. Mater. Chem. B*, 2022, **11**, 1029–1043.
6 S. A. Ansari, Z. Khatoon, N. Parveen, H. Fouad, A. Kulkarni, A. Umar, Z. A. Ansari and S. G. Ansari, *Sci. Adv. Mater.*, 2017, **9**, 2032–2038.
7 S. A. Ansari, A. Ahmed, F. K. Ferdousi, M. A. Salam, A. A. Shaikh, H. R. Barai, N. S. Lopa and M. M. Rahman, *J. Electroanal. Chem.*, 2019, **850**, 113394.
8 S. Malik, J. Singh, K. Saini, V. Chaudhary, A. Umar, A. A. Ibrahim, S. Akbar and S. Baskoutas, *Anal. Methods*, 2024, **16**, 2777–2809.
9 A. Umar, S. Akbar, R. Kumar, J. N. O. Amu-Darko, S. Hussain, A. A. Ibrahim, M. A. Alhamami, N. Almehbad, T. Almas and A. F. Seliem, *Chemosphere*, 2024, **349**, 140838.
10 B. Sharma, S. Jain, A. Umar, S. Rani, S. Kumar, A. A. Ibrahim and N. Dilbaghi, *Chem. Phys. Impact*, 2024, **8**, 100470.
11 Y. A. Waghmare, V. N. Narwade, A. Umar, A. A. Ibrahim and M. D. Shirsat, *Chem. Phys. Impact*, 2024, **8**, 100419.
12 Y. Xia, J. Wang, Y. Zhang, L. Song, J. Ye, G. Yang and K. Tan, *Nanoscale*, 2012, **4**, 5954.
13 M. G. Bawendi, C. R. Kagan and C. B. Murray, *Annu. Rev. Mater. Sci.*, 2006, **30**, 545–610.
14 K. R. Singh, V. Nayak, J. Singh, A. K. Singh and R. P. Singh, *RSC Adv.*, 2021, **11**, 24722–24746.
15 G. Maheshwaran, M. Malai Selvi, R. Selva Muneeswari, A. Nivedhitha Bharathi, M. Krishna Kumar and S. Sudhahar, *Adv. Powder Technol.*, 2021, **32**, 1963–1971.
16 M. Salavati-Niasari, G. Hosseinzadeh and F. Davar, *J. Alloys Compd.*, 2011, **509**, 4098–4103.

17 M. Ranjbar and M. Yousefi, *J. Inorg. Organomet. Polym. Mater.*, 2014, **24**, 652–655.
18 Y. Wu, Y. Chen and J. Zhou, *Mater. Lett.*, 2013, **95**, 5–8.
19 M. Nieminen, M. Putkonen and L. Niinistö, *Appl. Surf. Sci.*, 2001, **174**, 155–166.
20 V. M. Lu, T. R. Jue and K. L. McDonald, *Sci. Rep.*, 2020, **10**, 1–12.
21 H. Niu, Q. Min, Z. Tao, J. Song, C. Mao, S. Zhang and Q. Chen, *J. Alloys Compd.*, 2011, **509**, 744–747.
22 J. Choi and Y. H. Chung, *J. Nanomater.*, 2016, **2016**, 1–13.
23 S. A. Ansari and N. Parveen, *MatSci Express*, 2024, **1**, 28–32.
24 G. Mao, H. Zhang, H. Li, J. Jin and S. Niu, *J. Electrochem. Soc.*, 2012, **159**, J48–J53.
25 G. Chen, B. Han, S. Deng, Y. Wang and Y. Wang, *Electrochim. Acta*, 2014, **127**, 355–361.
26 M. Ghiasi and A. Malekzadeh, *Superlattices Microstruct.*, 2015, **77**, 295–304.
27 U. Rambabu and S. Do Han, *Ceram. Int.*, 2013, **39**, 701–708.
28 M. Zhang, W. Wang, P. Yuan, C. Chi, J. Zhang and N. Zhou, *Chem. Eng. J.*, 2017, **330**, 1137–1147.
29 T. Grzyb and S. Lis, *J. Rare Earths*, 2009, **27**, 588–592.
30 J. Kim, J. H. Lee, H. An, J. Lee, S. H. Park, Y. S. Seo and W. H. Miller, *Mater. Res. Bull.*, 2014, **57**, 110–115.
31 J. M. Vargas, J. J. Blostein, I. Sidelnik, D. Rondón Brito, L. A. Rodríguez Palomino and R. E. Mayer, *J. Instrum.*, 2016, **11**, 1–16.
32 T. Yamada, S. Shinoda and H. Tsukube, *Chem. Commun.*, 2002, 1218–1219.
33 G. Sivakumar, A. Gupta, A. Babu, P. K. Sasmal and S. Maji, *J. Mater. Chem. B*, 2024, **12**, 4724–4735.
34 Y.-Y. Chen, D. Kurniawan, S. M. Mousavi, P. V. Fedotov, E. D. Obraztsova and W.-H. Chiang, *J. Mater. Chem. B*, 2022, **10**, 9654–9661.
35 K. Dutta, K. Sarkar, S. Karmakar, B. Gangopadhyay, A. Basu, S. Bank, S. De, B. Das, M. Das and D. Chattopadhyay, *J. Mater. Chem. B*, 2023, **11**, 9478–9495.
36 H. Chen, Z. Cai, J. Gui, Y. Tang, P. Yin, X. Zhu, Y. Zhang, H. Li, M. Liu and S. Yao, *J. Mater. Chem. B*, 2023, **11**, 1279–1287.
37 Q. Liang, F. Yu, H. Cai, X. Wu, M. Ma, Z. Li, A. C. Tedesco, J. Zhu, Q. Xu and H. Bi, *J. Mater. Chem. B*, 2023, **11**, 2466–2477.
38 Y. C. Yeh, S. T. Kim, R. Tang, B. Yan and V. M. Rotello, *J. Mater. Chem. B*, 2014, **2**, 4610–4614.
39 E. A. Kataev, *Chem. Commun.*, 2023, **59**, 1717–1727.
40 S. H. Hewitt and S. J. Butler, *Chem. Commun.*, 2018, **54**, 6635–6647.
41 H. Zhang, J. Wang, S. Wei, C. Wang, X. Yin, X. Song, C. Jiang and G. Sun, *J. Mater. Chem. B*, 2023, **11**, 6082–6094.
42 Y. Zhang, H. Qin, Y. Huang, F. Zhang, H. Liu, H. Liu, Z. J. Wang and R. Li, *J. Mater. Chem. B*, 2021, **9**, 4654–4662.
43 L. Yang, P. Ma, X. Chen, Z. Cheng and J. Lin, *J. Mater. Chem. B*, 2022, **10**, 1386–1392.
44 S. C. G. and R. G. Balakrishna, *J. Mater. Chem. B*, 2023, **11**, 2184–2190.
45 Y. Yuan, X. S. Yan, X. R. Li, J. L. Cao, Z. Li and Y. B. Jiang, *Chem. Commun.*, 2017, **53**, 13137–13140.
46 M. Hu and G. Feng, *Chem. Commun.*, 2012, **48**, 6951.
47 C. M. G. Dos Santos, P. B. Fernández, S. E. Plush, J. P. Leonard and T. Gunnlaugsson, *Chem. Commun.*, 2007, 3389–3391.
48 Z. Guo, I. Shin and J. Yoon, *Chem. Commun.*, 2012, **48**, 5956–5967.
49 R. De, K. W. Jo, B. H. Lee, S. Some and K.-T. Kim, *J. Mater. Chem. B*, 2023, **11**, 6024–6043.
50 M. Devi, B. Raut and S. Sharma, *Part. Part. Syst. Charact.*, 2023, **40**, 1–18.
51 H. S. Mansur, A. A. P. Mansur, E. Curti and M. V. De Almeida, *J. Mater. Chem. B*, 2013, **1**, 1696.
52 P. Behera, K. Jaiswal and M. De, *Luminescence*, 2022, **37**, 2022–2035.
53 Z. Bin Shang, S. Hu, Y. Wang and W. J. Jin, *Luminescence*, 2011, **26**, 585–591.
54 Y. Lou, Y. Zhao and J. J. Zhu, *Nanoscale Horiz.*, 2016, **1**, 125–134.
55 J. F. Callan, R. C. Mulrooney, S. Kamila and B. McCaughan, *J. Fluoresc.*, 2008, **18**, 527–532.
56 X. Lou, D. Ou, Q. Li and Z. Li, *Chem. Commun.*, 2012, **48**, 8462–8477.
57 G. Leménager, S. Tusseau-Nenez, M. Thiriet, P. E. Coulon, K. Lahlil, E. Larquet and T. Gacoin, *Nanomaterials*, 2019, **9**, 1–14.
58 J. B. Brady, R. M. Newton and S. J. Boardman, *J. Geol. Educ.*, 1995, **43**, 466–470.
59 J. F. Watts and J. Wolstenholme, *An Introduction to Surface Analysis by XPS and AES*, Wiley, 2003.
60 L. Schlapbach and H. R. Scherrer, *Solid State Commun.*, 1982, **41**, 893–897.
61 L. Schlapbach, J. Osterwalder and H. C. Siegmann, *J. Less-Common Met.*, 1982, **88**, 291–297.
62 W. Witt, H. Geers and L. Aberle, *PARTEC 2004*, 2004, vol. 1, pp. 1–4.
63 P. W. Brazis, *Quantum Dots and Their Potential Impact on Lighting and Display Applications*, 2017.
64 A. N. Acharya and A. Sahoo, *J. Mater. Sci.*, 2023, **58**, 12976–12992.
65 X. L. Wu, J. Y. Fan, T. Qiu, X. Yang, G. G. Siu and P. K. Chu, *Phys. Rev. Lett.*, 2005, **94**, 1–4.
66 J. Y. Fan, H. X. Li, Q. J. Wang, D. J. Dai and P. K. Chu, *Appl. Phys. Lett.*, 2011, **98**, 081913.
67 C. H. Voon, B. Y. Lim and L. N. Ho, in *Synthesis of Inorganic Nanomaterials: Advances and Key Technologies*, Woodhead Publishing, 2018, pp. 213–253.
68 V. V. Zhirnov and R. K. Cavin, in *Microsystems for Bioelectronics*, *William Andrew Publishing*, 2015, pp. 19–49.
69 A. A. Mamaeva, V. I. Martynov, S. M. Deyev and A. A. Pakhomov, *Chemosensors*, 2022, **10**, 1–8.
70 V. D. Paramita, N. Panyoyai and S. Kasapis, *Int. J. Mol. Sci.*, 2020, **21**, 2550.
71 C.-S. Chu, M.-W. Hsieh and Z.-R. Su, *MATEC Web Conf.*, 2016, **59**, 01001.
72 S. Majhi, R. Singh, C. S. P. Tripathi and D. Guin, *New J. Chem.*, 2024, **48**, 7904–7910.

73 L. Wu, W. Pan, H. Ye, N. Liang and L. Zhao, *Colloids Surf., A*, 2022, **638**, 128330.
74 Y. Xia, J. Wang, Y. Zhang, L. Song, J. Ye, G. Yang and K. Tan, *Nanoscale*, 2012, **4**, 5954–5959.
75 H. J. B. Silva, C. F. Pereira, G. Pereira and G. A. L. Pereira, *Micromachines*, 2024, **15**, 373.
76 J.-L. Chen and C.-Q. Zhu, *Anal. Chim. Acta*, 2005, **546**, 147–153.
77 Y. Chen and Z. Rosenzweig, *Anal. Chem.*, 2002, **74**, 5132–5138.
78 S. Veerasingam and R. Venkatachalapathy, *Infrared Phys. Technol.*, 2014, **66**, 136–140.
79 R. Serrano-Bayona, C. Chu, P. Liu and W. L. Roberts, *Materials*, 2023, **16**, 1192.
80 F. J. Millero, *Geochim. Cosmochim. Acta*, 1992, **56**, 3123–3132.
81 Y. Xiong, *Appl. Geochem.*, 2011, **26**, 1130–1137.
82 F. I. Sergeevich, L. T. Evgenievna, L. D. Sergeevich and A. A. Alexandrovich, *Arab J. Basic Appl. Sci.*, 2022, **29**, 1–9.